https://doi.org/10.5194/egusphere-2026-3283
Preprint. Discussion started: 3 August 2026

Quantifying the Role of Sea Ice in Seasonal and Interannual Variability in Surface Stress and Mixed-Layer Entrainment in the Central Canada Basin

Elizabeth Bailey[1], Annika Margevich[1], and Mary-Louise Timmermans[1]

[1]Department of Earth and Planetary Sciences, Yale University

Correspondence: Elizabeth Bailey (elizabeth.bailey@yale.edu)

Abstract. Over the last few decades, the Beaufort Gyre region (BGR) has experienced significant ice loss, leading to changes in momentum transfer within the atmosphere-ice-ocean system. We evaluate monthly and interannual variability of surface stress in the BGR, and a sub-region (the Central Canada Basin, CCB) within it, from 2003–2023. We find an increase in surface-ocean stress magnitude in the CCB of $0.007 \pm 0.001\ \mathrm{N\,m^{-2}}$ per decade, with the largest linear increases in November–December. We demonstrate that the shifting sea-ice regime, characterized by greater mobility and increased responsiveness to wind forcing, is the primary driver of increased surface-ocean stress, as opposed to changes in the wind field itself. Anomalously High-Stress Events (HSEs, characterized by stress magnitudes an order of magnitude larger than background levels) in the CCB occur most frequently in fall and have increased in frequency over 2003–2023, contributing to an increase in annual time-integrated surface stress of $0.54 \pm 0.45\ \mathrm{N\,m^{-2}}$ per decade during HSEs. We examine the implications of increased sea-ice mobility and changing surface-ocean stresses on the ocean mixed layer using an energy-balance entrainment parameterization. We find that stress-driven entrainment can account for ∼65% of October–March deepening, while buoyancy-driven processes contribute ∼7% of deepening during freeze-up. Mechanical mixing during HSEs contributes to ∼28% of all stress-induced mixing, even though HSEs occur less than 7% of the time during the 2003–2023 period. In November and December, the only months with statistically significant increases in surface stress, we estimate that increased surface stress can account for ∼0.15 and $0.1\ \mathrm{m\,year^{-1}}$ more deepening in each month over 2003–2019. This is ∼20% of the observed ∼0.7 and $0.6\ \mathrm{m\,year^{-1}}$ increased deepening in November and December over the CCB for 2003–2019, and we infer that other physical processes dominate the observed mixed-layer deepening trend. These results highlight how sea-ice decline and mobility enhance momentum transfer, suggesting a potential mechanism for a positive feedback via increased ocean-to-ice heat fluxes.

1 Introduction

Changes in the Arctic atmosphere-ice-ocean system most notably include the thinning of Arctic sea ice and decreases in its concentration and extent. September Arctic sea ice extent has declined by about 46% from 1979 to 2024 (Thoman et al., 2025), with some of the largest losses in both thickness and extent occurring in the Canada Basin's Beaufort Gyre Region (BGR; Figure 1, bounded by the dotted black line; Babb et al., 2022). In addition to changes in the sea ice pack, changes in the upper ocean have also been observed; significant accumulations of ocean freshwater and heat in the BGR were observed from 2003

https://doi.org/10.5194/egusphere-2026-3283
Preprint. Discussion started: 3 August 2026

through 2019, while the following five years saw declines in both (Proshutinsky et al., 2019; Timmermans et al., 2025). Ocean mixed-layer properties have also evolved; BGR mixed-layer salinity increased by $\sim$1 $\mathrm{g\,kg^{-1}}$ between the 2006–2012 and 2013–2017 periods, which occurred alongside reduced stratification and $\sim$9 m of mixed-layer deepening (Cole and Stadler, 2019; Liu and Yu, 2025). Mixed-layer depths and upper ocean stratification are strongly linked to ocean heat content in the BGR, with its potential to influence sea ice, as significant heat is stored in a warm layer that resides immediately below the base of the mixed layer (Timmermans et al., 2018). Strong stratification at the mixed-layer base generally inhibits vertical heat fluxes from the warm layer into the surface mixed layer in the BGR (Toole et al., 2010). However, Zhong et al. (2022) found that BGR ocean-to-ice heat fluxes increased from 0.76 ± 0.05 $\mathrm{W\,m^{-2}}$ during 2006–2012 to 1.63 ± 0.08 $\mathrm{W\,m^{-2}}$ during 2013–2018, attributing this increase primarily to enhanced convection as a result of increased ice growth.

Rainville and Woodgate (2009) suggested that decreased sea-ice cover could result in a more energetic Arctic Ocean via increased wind energy input to the surface ocean, which could lead to increased mixing and therefore increased vertical heat fluxes. Quantifying ocean surface stress in the Arctic is especially complex due to sea ice modulating momentum transfer to the surface ocean, and sea ice losses significantly influence surface stresses, which have been found to increase over the past two decades (e.g., Martin et al., 2014; Muilwijk et al., 2024; Liu and Yu, 2025). Liu and Yu (2025) found wintertime (i.e., mostly under sea ice) average increases in ocean surface stress of approximately 0.005 $\mathrm{N\,m^{-2}}$ (around 50%) when comparing the 2003–2012 and 2013–2022 periods in the BGR. It has not been quantified how increased stresses may have played a role in the mixed-layer deepening shown by Cole and Stadler (2019) and Liu and Yu (2025).

Episodes of anomalously high stress (e.g., storms) may play an out-sized role in stress input, and the associated entrainment of vertical heat, to the surface ocean (Yang et al., 2001; Peng et al., 2021). Extreme wind events have been shown to drive sufficient mechanical mixing to penetrate the base of the mixed layer, even in strongly stratified conditions (Yang et al., 2001, 2004; Peng et al., 2021). While observations of mixed-layer deepening during the course of a storm are sparse, the influence of storm mixing on ocean-to-ice heat fluxes has been inferred from observed sea ice loss during events (e.g., Zhang et al., 2013).

Here, we analyze how the evolving state of the sea-ice pack regulates momentum transfer from the atmosphere to the ocean in the BGR for the period 2003–2023, and relate our findings to ocean mixed-layer observations. We focus on a sub-region of the BGR, the Central Canada Basin (CCB; Figure 1, red box), which exhibits less spatial variability (i.e., associated with basin boundary regions) than the larger BGR, although we will show that mean ocean stresses in the CCB are a good representation of stresses in the broader BGR. We also characterize episodes of anomalously high stress in the CCB and compare the inferred upper-ocean response during these episodic events to that under background conditions. We analyze Ice-Tethered Profiler (ITP) measurements to characterize the monthly to decadal evolution of mixed-layer properties, including mixed-layer depth, density difference across the mixed-layer base, and maximum stratification at the mixed-layer base. Surface ocean stresses and ice-growth-rate estimates from moorings in the CCB, as well as mixed-layer properties, are used together with an energy-balance entrainment parameterization to estimate both shear- and buoyancy-driven entrainment rates. We compare these rates to observed mixed-layer depth changes to explore the extent to which surface stress drives seasonal and interannual changes in mixed-layer depth.

https://doi.org/10.5194/egusphere-2026-3283
Preprint. Discussion started: 3 August 2026

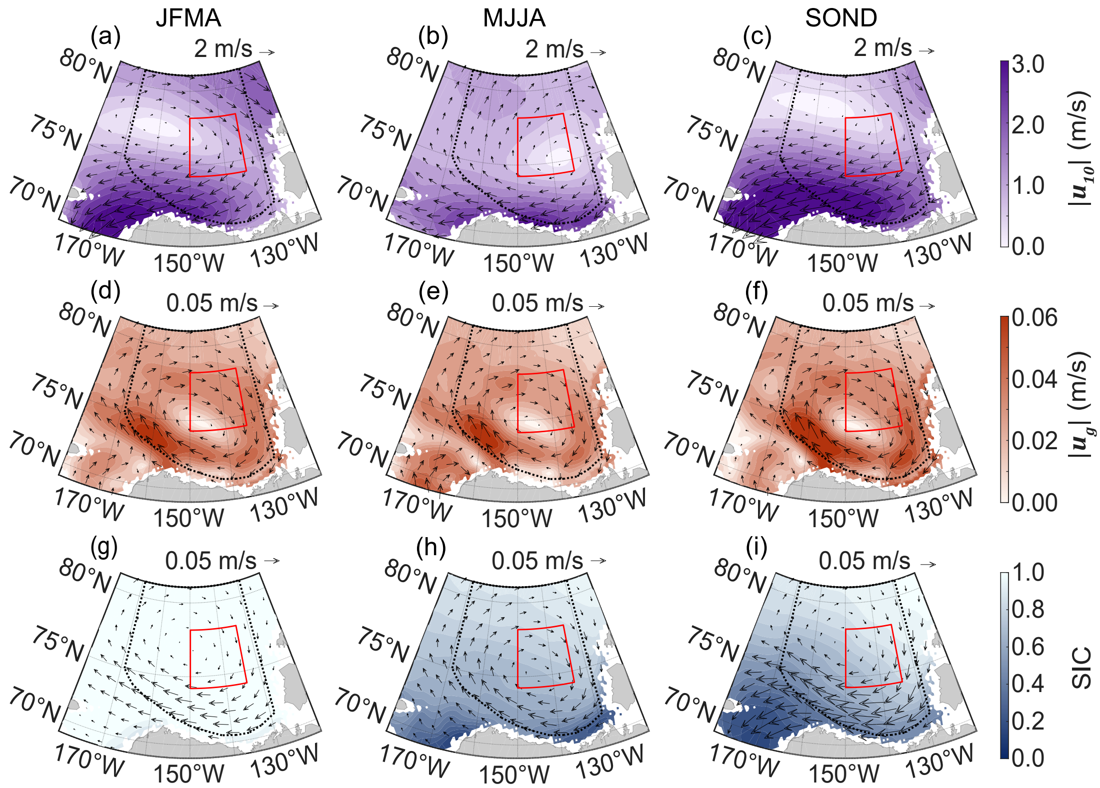

Figure 1. Mean 10 m wind velocity ($\boldsymbol{u_{10}}$) over 2003-2023 for a) January–April (JFMA), b) May–August (MJJA), and c) September–December (SOND). Mean geostrophic velocity ($\boldsymbol{u_g}$) for 2003–2023 in d) JFMA, e) MJJA, and f) SOND. Mean ice velocity ($\boldsymbol{u_i}$; arrows) and sea ice concentration (SIC; colors) for 2003–2023 in g) JFMA, h) MJJA, and i) SOND. The red box indicates the Central Canada Basin (CCB), and the region encompassed by the black dotted line indicates the Beaufort Gyre Region (BGR).

A brief summary of the paper is as follows. In Section 2, we introduce the methods and data used to calculate surface stress and to characterize anomalously high-stress events. In Section 3, we analyze seasonal and interannual variability of surface-ocean stress in the CCB. In Section 4, we introduce the oceanographic observations and mixed-layer entrainment parameterization, and examine the observed evolution of mixed-layer depth as it compares to that inferred from the parameterization. Section 5 provides a summary and discussion of our results.

2 Surface stress in the Central Canada Basin

Here, we introduce the datasets and methodology for calculating surface-ocean stresses and outline our characterization of high-stress events. Surface-ocean stresses require winds, ocean geostrophic velocities, sea-ice velocity, and sea ice concentration.

https://doi.org/10.5194/egusphere-2026-3283
Preprint. Discussion started: 3 August 2026

2.1 Datasets

Wind velocity is from the ERA5 reanalysis data product with an hourly temporal resolution and a 0.25° by 0.25° spatial resolution (Hersbach et al., 2018). We use daily mean values and linearly interpolate the data onto the 25 km EASE-Grid (e.g., Meneghello et al., 2018). In comparison with *in situ* ship-based Arctic observations, ERA5 10 m winds consistently had the highest correlation ($R > 0.9$) among 6 different reanalysis products (Graham et al., 2019); the uncertainty associated with this product is estimated as a root-mean-square error between 0.9 and 1.4 $\mathrm{m\,s^{-1}}$ depending on the season (Graham et al., 2019).

The large-scale surface wind field in the BGR is dominated by the Beaufort High, an anticyclonic, atmospheric high centered over the Canada Basin, which exhibits broad seasonal changes (Figure 1a–c; Serreze and Barrett, 2011; Timmermans and Toole, 2023). In the fall and early winter, surface winds are typically fastest, particularly in the southern portion of the BGR (Figure 1c). The wind field has not changed significantly from 2003–2023, with the exception of statistically significant wind speed increases in the central-north BGR and decreases in the southern BGR in September–December (Figure S1a–c).

Surface geostrophic currents are provided by the Centre for Polar Observation and Modeling (CPOM), and are derived from Dynamic Ocean Topography (DOT) fields from the Envisat and CryoSat-2 missions (Armitage et al., 2016, 2017; Lin et al., 2023). The CPOM DOT data are available in two datasets: 1) for 2003 to 2014, with spatial coverage from 60°N to 81.5°N (Armitage et al., 2016), and 2) for 2011 through 2020, with spatial coverage from 60°N to 88°N (Lin et al., 2023), where Lin et al. (2023) follows the methods of (Armitage et al., 2016, 2017). We use the first dataset for 2003 through 2010 and the latter for 2011 through 2020 (datasets agree well in the overlapping period). Datasets have a monthly temporal resolution and spatial resolution of 0.75° × 0.25°, which we interpolate onto the 25 km EASE-Grid. For the period 2021 to 2023, we estimate the surface geostrophic currents from DOT from ICESat-2 provided by the National Snow and Ice Data Center (NSIDC; Morison et al., 2025). These data are provided at a monthly resolution and on a polar stereographic grid with nominal 25 km grid spacing covering up to 88°N. The corresponding geostrophic velocity fields are not provided in this dataset, and we calculate those here by first applying a 2-D Gaussian smoothing kernel with a standard deviation of 4 grid cells to the monthly DOT fields. From there, we re-grid monthly DOT onto a 0.75° × 0.25° grid and calculate DOT gradients in latitudinal and longitudinal directions using centered differences. Geostrophic velocities are then calculated via geostrophic balance. Finally, we re-grid the estimated geostrophic velocity fields onto the 25 km EASE grid. DOT-estimates of geostrophic velocity compared to in situ Acoustic Doppler Current Profiling velocities in the CCB indicate mean differences between ∼0.2 and ∼0.5 $\mathrm{cm\,s^{-1}}$ (Armitage et al., 2017).

Climatological geostrophic ocean flow clearly shows the Beaufort Gyre, driven by the anticyclonic winds of the Beaufort High, is the dominant flow feature in the region (Figure 1d–f; Proshutinsky et al., 2002, 2009). Mean monthly geostrophic currents in the BGR are about 1 to 4 $\mathrm{cm\,s^{-1}}$ (Figure 1d–f). The geostrophic Beaufort Gyre is a stable feature that persists in all months (Figure 1d–f). Geostrophic current speeds have increased with statistically significant trends across all seasons over the 2003–2023 period, predominantly in the southern and western BGR, where geostrophic flow is typically fastest (Figure S1d–f).

https://doi.org/10.5194/egusphere-2026-3283
Preprint. Discussion started: 3 August 2026

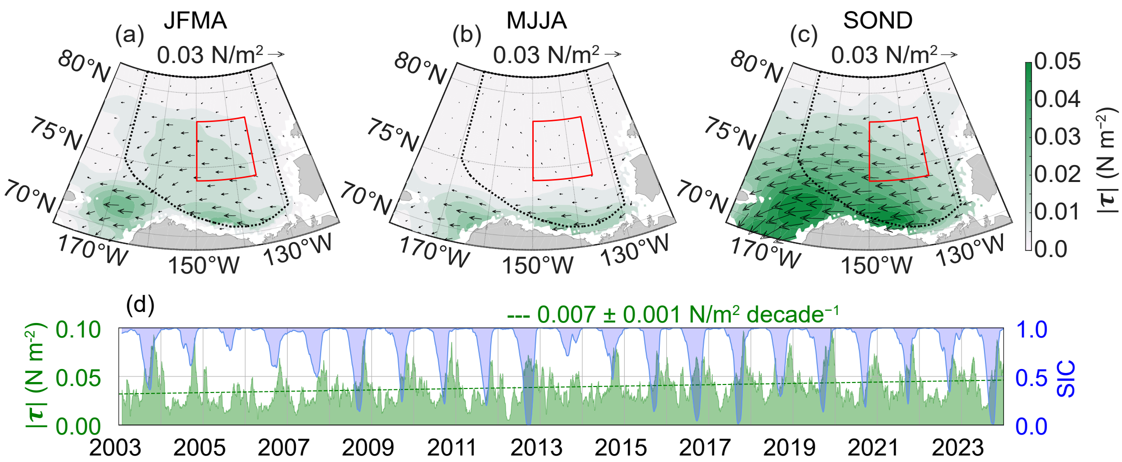

Figure 2. Mean total surface ocean stress ($\boldsymbol{\tau}$) for 2003–2023 in a) January–April (JFMA), b) May–August (MJJA), and c) September–December (SOND). Arrows indicate the magnitude and direction of the surface stress vector. The red box indicates the Central Canada Basin (CCB) and the black region indicates the Beaufort Gyre region (BGR). d) 30-day running mean timeseries of the mean magnitude of total surface stress ($|\boldsymbol{\tau}|$; green) and sea ice concentration (SIC; blue) over the Central Canada Basin (CCB) from 2003–2023. The linear trend for $|\boldsymbol{\tau}|$ with 95% confidence interval is given.

Sea ice velocity is from the Polar Pathfinder Daily 25 km EASE-Grid Sea Ice Motion Vectors, Version 4 (Tschudi et al., 2019). Uncertainty is $\sim$8% of the observed in situ ice drift (Zhang and Rothrock, 2003). Sea ice concentration (SIC) is from Nimbus-7 SMMR and DMSP SSM/I-SSMIS Passive Microwave Data Version 2 (DiGirolamo et al., 2022), interpolated onto the 25 km EASE-Grid. Uncertainties associated with sea-ice concentration (SIC) are $\leq$5% (DiGirolamo et al., 2022).

Sea ice drift in the region of study follows a large-scale anticyclonic circulation, with drift speeds ranging from a few centimeters per second to several tens of centimeters per second (Figure 1g–i). Drift speeds are fastest in the September through December period (Figure 1i). Seasonal trends in sea-ice speed indicate a general increase in the BGR over the 2003-2023 period, with statistically significant trends in the western BGR in JFMA and northern BGR in MJJA and SOND (Figure S1g–i); Petty et al. (2016) noted that ice drift speeds in the BGR increased over 2000-2013 by an amount more than would be expected from the trend in surface winds. With respect to SIC, in January through April, there are weak, yet statistically significant, increasing trends in the central and eastern BGR from 2003 through 2023 (Figure S1j). For the rest of the year, SIC has been decreasing for the 2003–2023 period, particularly in the central BGR in September through December (Figure S1k–l).

2.2 Calculating surface-ocean stress

Surface-ocean stress calculations follow previous studies (Meneghello et al., 2017, 2018). The total stress on the ocean surface, $\boldsymbol{\tau}$, is given as the sum of the ice-ocean stress, $\boldsymbol{\tau}_i$, and the air-ocean stress, $\boldsymbol{\tau}_a$, where each may be represented by a quadratic

https://doi.org/10.5194/egusphere-2026-3283
Preprint. Discussion started: 3 August 2026

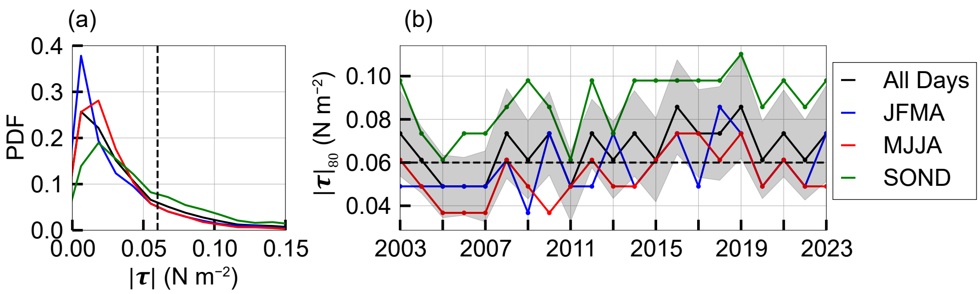

Figure 3. a) Probability density functions for the magnitude of daily surface stress ($|\boldsymbol{\tau}|$) for all days (black), January–April (blue), May–August (red), and September–December (green) in the Central Canada Basin (CCB) for 2003–2023. b) The magnitude of surface stress at the 80th percentile ($|\boldsymbol{\tau}|_{80}$) of each annual distribution of $|\boldsymbol{\tau}|$ for all days (black), January–April (blue), May–August (red), and September–December (green). The shaded region represents the annual mean standard deviation over the CCB. The dashed lines at $|\boldsymbol{\tau}|$=0.06 $\mathrm{N\,m^{-2}}$ in both panels represent the threshold for a high-stress event (HSE).

drag law and weighted by SIC as follows

$$\boldsymbol{\tau} = SIC\rho_0 C_{Di}|\boldsymbol{u_{rel}}|(\boldsymbol{u_{rel}}) + (1 - SIC)\rho_a\, C_{Da}|\boldsymbol{u_{10}}|(\boldsymbol{u_{10}}), \tag{1}$$

where $\rho_0 = 1028\ \mathrm{kg\,m^{-3}}$ and $\rho_a = 1.25\ \mathrm{kg\,m^{-3}}$ are reference densities of seawater and air, respectively, C_{Di} and C_{Da} are ice-ocean and air-ocean drag coefficients, $\boldsymbol{u_{10}}$ is the 10 m wind velocity, and $\boldsymbol{u_{rel}}$ is the ice-ocean relative velocity, given by

$$\boldsymbol{u_{rel}} = \boldsymbol{u_i} - (\boldsymbol{u_g} + \boldsymbol{u_e}). \tag{2}$$

Here, $\boldsymbol{u_i}$ is the sea-ice velocity, $\boldsymbol{u_g}$ is the geostrophic velocity, and $\boldsymbol{u_e}$ is the Ekman velocity. We use a surface Ekman velocity that is rotated 45° to the right of the surface stress, given by

$$\boldsymbol{u_e} = \frac{\boldsymbol{\tau}\sqrt{2}e^{-i(\pi/4)}}{f_0\rho_0 D_e}, \tag{3}$$

where $f_0 = 1.46\ \times\ 10^{-4}\ \mathrm{s^{-1}}$ is the Coriolis parameter at the central latitude of our study region (76°N), and D_e is the Ekman depth taken to be 20 m following Yang (2006). Since $\boldsymbol{\tau}$ and $\boldsymbol{u_e}$ are dependent on each other, (1), (2), and (3) must be solved iteratively. We assume an initial value of $\boldsymbol{u_e} = 0$ and take $|\boldsymbol{u_{rel}}| \leq 0.5\ \mathrm{m\,s^{-1}}$ to prevent anomalously large $\boldsymbol{\tau}$; this affects fewer than 5% of the values.

While each dataset used to calculate surface stress has uncertainties, the chosen drag coefficients also have uncertainty. Here we use a canonical value of $C_{Di} = 5.5 \times 10^{-3}$ based on the work of Mcphee (1980); however, values may range from 1 to 10 $\times\ 10^{-3}$ (Cole et al., 2017; Brenner et al., 2021). For the air-ocean drag coefficient, we take $C_{Da} = 1.25\ \times\ 10^{-3}$, although this has been estimated to vary between 0.3 and 1.5 $\times\ 10^{-3}$ (Large and Pond, 1981; Geernaert, 1987). The constant values taken here are for consistency with previous analyses of surface stress in the region (Meneghello et al., 2017, 2018; Dewey et al., 2018; Liu and Yu, 2025), with the recognition that this choice may be a significant point of uncertainty.

In general, surface-ocean stress is lowest in magnitude during May through August, and highest in September through December (Figure 2a–c). In each season, the highest values are generally in the southern BGR (Figure 2a–c). In the less

https://doi.org/10.5194/egusphere-2026-3283
Preprint. Discussion started: 3 August 2026

spatially variable CCB, surface stress has generally increased at a rate of 0.007 ± 0.001 $\mathrm{N\,m^{-2}}$ per decade over 2003–2023 (Figure 2d). Compared with the BGR, the CCB has approximately the same mean monthly values (∼0.03–0.06 $\mathrm{N\,m^{-2}}$) and seasonal cycle, as well as general interannual variability, making it a representative subregion with less spatial variability (Figures S2 and S3). The monthly means and interannual variability of surface stress in the CCB will be discussed in detail in Section 3.1.

2.3 Characterizing high-stress events

In this section, we characterize episodic high-stress events, which potentially lead to anomalously high momentum input to the upper ocean. Across all seasons, the most frequent surface stress magnitudes are ∼0.020 $\mathrm{N\,m^{-2}}$ (Figure 3a). At the upper tail of the distribution, the top 20% of ocean stress values exceed 0.06 $\mathrm{N\,m^{-2}}$, which corresponds to the 80th percentile threshold computed from all days over 2003–2023 (Figure 3b). We use this value to define a high-stress event (HSE) as a period when the daily spatially-averaged $|\boldsymbol{\tau}|$ is ≥0.06 $\mathrm{N\,m^{-2}}$ for three or more consecutive days in the CCB. A minimum duration of 3 days is imposed to exclude transient synoptic events that are unlikely to drive significant oceanographic response. During the identified HSEs, an average of ∼82% of the individual stress values within the CCB exceed 0.06 $\mathrm{N\,m^{-2}}$ (i.e., the spatial averaging is appropriate).

There are alternative ways to define a high-stress event. For example, identification of polar lows is another approach (Stoll, 2022b). However, Stoll (2022b) identify only 3 polar lows in the CCB over 2003–2020, and these were not consistently concurrent with high surface stress magnitudes (Stoll, 2022a). A fundamental challenge is that sea ice cover moderates the transfer of wind momentum into the ocean such that an intense cyclone may not lead to significant momentum transfer if extensive sea ice is not responsive to wind forcing, and direct evaluation of the surface stress magnitude is necessary. In Section 3.2, we discuss surface conditions during high-stress events and their occurrence. In Section 4.3, we discuss the potential influence of HSEs on mixed-layer entrainment.

3 Interannual and seasonal variability in surface stresses

In this section, we investigate the seasonal cycle of ocean surface stress over the CCB using the mean values from individual months, and characterize the monthly linear trends (over 2003–2023) in both stress and each of the contributing factors.

3.1 Monthly mean stresses over the CCB

We first characterize each of the factors that contribute to the mean surface ocean stresses over the CCB: winds, sea ice concentration (SIC), sea-ice motion, and ocean geostrophic flow. Wind speed magnitudes are weakest from May through August, and typically strongest in early fall (Figure 4a). Over 2003–2023, we do not find statistically significant linear trends in monthly winds, with the possible exception of March, where wind speeds show an increase of 0.34 ± 0.32 $\mathrm{m\,s^{-1}}$ per decade (Figure S4a).

https://doi.org/10.5194/egusphere-2026-3283
Preprint. Discussion started: 3 August 2026

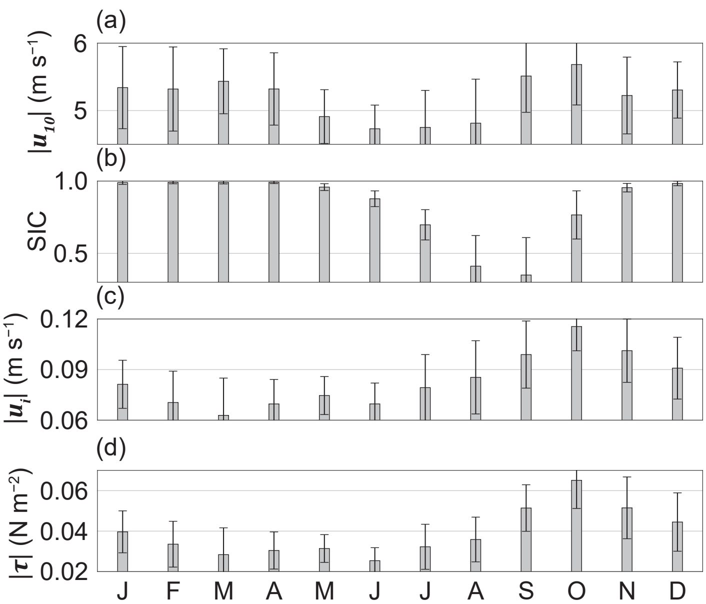

Figure 4. Monthly mean a) 10 m wind speed ($|\boldsymbol{u_{10}}|$), b) sea ice concentration (SIC), c) sea-ice drift speed ($|\boldsymbol{u_i}|$), and d) magnitude of total surface stress ($|\boldsymbol{\tau}|$) over the CCB for the 2003-2023 period. Error bars indicate one interannual standard deviation.

Sea ice drift speeds are generally slowest from February through June when SIC is maximal, and increase in July to September when SIC is lower, and the ice pack is more mobile (Figure 4b,c). Notably, winds are weak in July and August, while internal ice stresses are also weak. Statistically significant linear increases in drift speeds over 2003–2023 are observed for March–June and November–December (Figure S4b). These may be considered the shoulder seasons when the overall thinning and weakening of the ice pack is most apparent, even while SIC may not be changing appreciably. Normalizing ice-drift speed by wind speed clearly demonstrates this increased mobility; statistically significant linear trends in $\frac{|\boldsymbol{u_i}|}{|\boldsymbol{u_{10}}|}$ are observed in all months except August through October (Figure 5b). These findings suggest that the increase in sea ice drift is primarily attributable to reduced resistance of the ice pack to wind forcing (see e.g., Petty et al., 2016).

Winds, ice motion, and SIC combine to produce the distinct seasonal cycle of surface ocean stress in the CCB. Although including geostrophic flow is key when quantifying ocean surface stress (e.g., Zhong et al., 2018), it exhibits little seasonality. The interplay between atmospheric forcing and sea ice conditions gives rise to the seasonality of surface stress magnitude; for example, the combination of strong winds, high ice mobility, and higher concentrations (between 80–90%) results in strong ocean stress in fall. In the CCB, ocean stress magnitude is largest from September through December and smallest from ∼March through August (Figure 4d). Analyses using the Pan-arctic Ice-Ocean Modeling and Assimilation System (PIOMAS) have shown that momentum transfer is maximized for an SIC of 80–90% because ice-ocean stress is more effective at this transfer than air-ocean stress, while internal ice stresses lead to reduced ice motion when SIC>90% (Martin et al., 2014). We find a similar optimal SIC for momentum transfer in the fall (when SIC spans a full range in our data). September–December

https://doi.org/10.5194/egusphere-2026-3283
Preprint. Discussion started: 3 August 2026

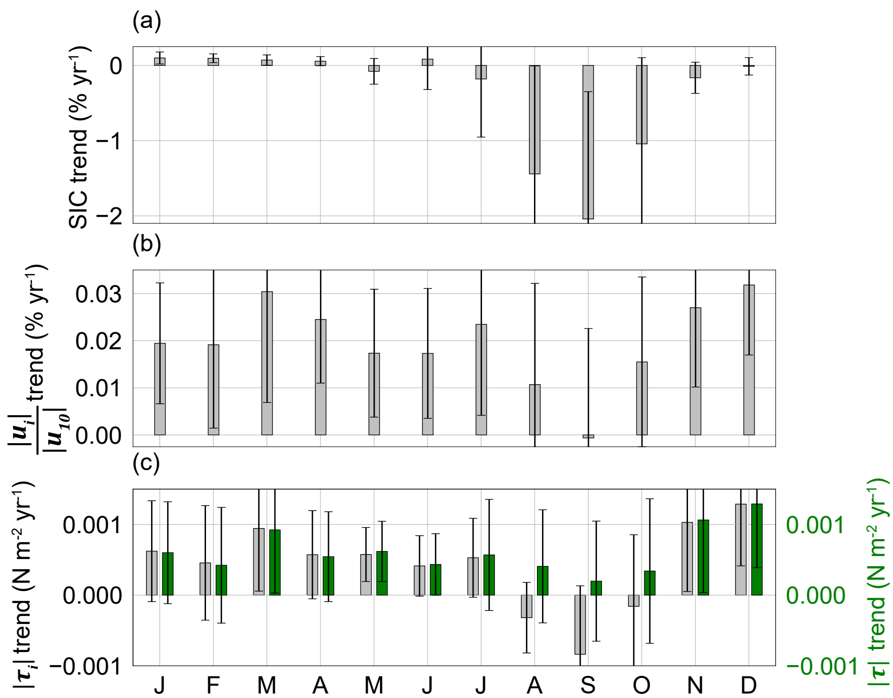

Figure 5. Monthly linear trends of a) mean sea ice concentration (SIC); b) mean sea-ice drift speed relative to wind speed ($\frac{|u_i|}{|u_{10}|}$); c) mean magnitude of ice-ocean surface ($|\tau_i|$, gray) and total surface ocean stress ($|\tau|$, green) over the CCB. Error bars indicate the 95% confidence interval of the linear trend.

ocean surface stress magnitude normalized by wind speed generally increases with SIC up to SIC ∼78% and decreases for further increases in SIC (Figure S5b).

In general, we see a linear increase over 2003–2023 in surface stress magnitude in the CCB (Figure 2d), most notably in March–May and November–December (Figure 5c, green bars). The largest increase is in December, with a linear trend of $0.013 \pm 0.009\ \mathrm{N\,m^{-2}}$ per decade (Figure 5c, green bars). This surface stress increase during winter months is consistent with previous studies in the region; Liu and Yu (2025) show a December–March surface stress increase averaging ∼0.005 $\mathrm{N\,m^{-2}}$ between 2003–2012 and 2013–2022. Similarly, Martin et al. (2014) report that simulated ocean-surface stress exhibits its largest increase in October–December ($0.007\ \mathrm{N\,m^{-2}}$ per decade over the 1979–2012 period).

In months with low SIC (August–October), we find no statistically significant change in surface-ocean stress over 2003–2023 (Figure 5c). For the 1979–2012 period, Martin et al. (2014) find decreasing interannual trends in surface-ocean stress during low SIC months, with modeled July–September surface stresses decreasing by $\sim 0.002\ \mathrm{N\,m^{-2}}$ per decade (Martin et al., 2014). The discrepancy with our results likely reflects the different time periods, with the earlier 1979–2012 record encompassing a period of more rapid sea-ice decline (e.g., Stern, 2025).

Increases in sea-ice drift speed (attributed to increased pack mobility as opposed to increased wind speeds) can explain the increases in surface stress during ice-covered months in the CCB (Figure 5c, compare green and gray bars). The relationship

https://doi.org/10.5194/egusphere-2026-3283
Preprint. Discussion started: 3 August 2026

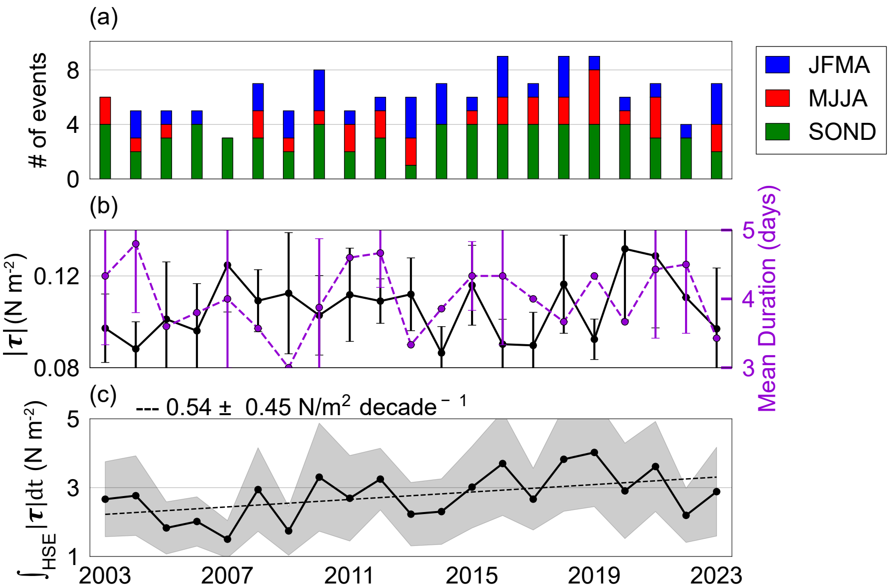

Figure 6. a) Number of high-stress events (HSEs) in the Central Canada Basin (CCB) for January–April (blue), May–August (red), and September–December (green) from 2003–2023. The interannual linear trend with a 95% confidence interval is given. b) The mean surface stress magnitude ($|\boldsymbol{\tau}|$, black) and the mean duration of all HSEs in each year over the CCB from 2003–2023. Error bars indicate one median absolute deviation. c) Annual time-integrated surface stress magnitude for the entire year (black). Shading represents one spatial median absolute deviation of surface stress in the CCB during HSEs.

is particularly evident in November and December, when the $\sim$0.001 $\mathrm{N\,m^{-2}\,year^{-1}}$ trend in surface stress is accompanied by a $\sim$0.03 $\%\,\mathrm{year}^{-1}$ trend (or a 1.8% per year increase relative to the climatological mean of 0.017) in the ice to wind speed ratio over 2003–2023 (Figure 5c). Increases in the ice to wind speed ratio have been observed across the Arctic, with Zhang et al. (2022) reporting the largest trend of 2.3% per year relative to a climatological mean of 0.015 in autumn over the Beaufort Sea region for the 1979–2019 period. Our result agrees with the Arctic-wide finding of Martin et al. (2014), who find modeled annual linear surface stress increases of 0.006 N m^{-2} per decade from 2000 to 2012 primarily due to increased momentum transfer (rather than wind forcing). These authors highlight the increasing mobility of the ice pack as the primary mechanism behind increasing surface stress.

3.2 High-stress Events

In the previous section, we described area and monthly mean stress magnitudes in general. In this section, we turn to the high-stress events (HSEs; defined in Section 2.3) to examine the role of these short-term events in the monthly-averaged momentum input. Characterizing a HSE as a period when $|\boldsymbol{\tau}| \geq 0.06\ \mathrm{N\,m^{-2}}$ for ≥ 3 consecutive days yields $\sim$6 HSEs per year in the CCB over 2003–2023; the number has increased from $\sim$6 to $\sim$7 events per year between 2003–2012 and 2013–2023 (Figure

https://doi.org/10.5194/egusphere-2026-3283
Preprint. Discussion started: 3 August 2026

6a). Seasonally, HSEs are more likely to occur in the fall, when their surface ocean stress magnitudes are also generally largest (Figure S6).

The mean surface stress magnitude during HSEs is ∼0.11 ± 0.03 $\mathrm{N\,m^{-2}}$ (Figures 6b and S6d). HSE wind speeds average around 7.9 ± 1.2 $\mathrm{m\,s^{-1}}$, with ice drift speeds ∼0.16 ± 0.04 $\mathrm{m\,s^{-1}}$ (Figure S6). These are ∼30 to 50% faster than their mean values (Figures 4 and S6). The average duration of each HSE is ∼4.0 ± 0.5 days, with little change to this over 2003–2023 (Figure 6b). We found no statistically significant change in HSE wind or ice speeds (nor in the ratio of their magnitudes), nor in HSE mean stress magnitudes in the CCB over 2003–2023 (Figures 6b and S7). While HSEs occur during only ∼7% of the days in the 2003–2023 period, they have a significant influence on momentum transfer in any given year, with approximately 20% of the annual time-integrated stress in any given year occurring during HSEs. While the characteristics of individual HSEs have remained largely consistent over time, their increased frequency has resulted in an increase in the time-integrated surface stress during HSEs of 0.54 ± 0.45 $\mathrm{N\,m^{-2}}$ per decade (Figure 6c). The influence of HSEs on mixed-layer entrainment will be explored in further detail in Section 4.4.

4 Drivers of Seasonal and Interannual Mixed Layer Variability

In this section, we examine how the surface stresses and sea-ice mobility characterized in the preceding sections influence the CCB mixed layer. We place entrainment at the base of the mixed layer, resulting from mechanical forcing, in context with convective mixed-layer deepening (and shoaling arising from ice melt), using estimates of surface buoyancy fluxes based on the sea-ice growth cycle.

4.1 Upper ocean and sea-ice thickness data

We assess the seasonal and interannual evolution of the mixed layer using temperature and salinity data from Ice-Tethered Profilers (ITPs) (individual profile locations are shown as gray dots, Figure 7a; Krishfield et al., 2008; Toole et al., 2011). An ITP drifts with its host ice floe, profiling the upper 700 m of the water column every ∼6 to 12 hours. This sampling frequency results in a horizontal resolution of less than 2.5 km on average, based on sea-ice drift speeds (Krishfield et al., 2008). Profiles are 1 m binned in the vertical. We focus on the CCB, which has a high concentration of profiles over the study period (2003–2023); approximately 17,000 profiles (Figure S8). In addition to ITP profiles, we analyze ship-based conductivity, temperature, and depth (CTD) data from the annual Beaufort Gyre Observing System (BGOS)/Joint Ocean Ice Study (JOIS) expeditions, which are limited to summer and fall months (Proshutinsky et al., 2019). BGOS/JOIS measurements provide spatially comprehensive measurements of the CCB each year, while ITP profiles provide year-round mixed-layer measurements (for mixed layers deeper than ∼7 m).

Buoyancy frequency ($N^2 = -(g/\rho_0)d\rho/dz$) is computed in the upper 50 m of the water column for each profile (this depth consistently exceeded the maximum mixed-layer depth). The maximum buoyancy frequency, N_m^2, in this depth range and its corresponding depth are computed. Mixed-layer depth ($z = H$) is taken to be two grid points (∼2 m) above the depth of N_m^2. This method of mixed-layer depth calculation yields statistically identical results to a criterion based on density difference

https://doi.org/10.5194/egusphere-2026-3283
Preprint. Discussion started: 3 August 2026

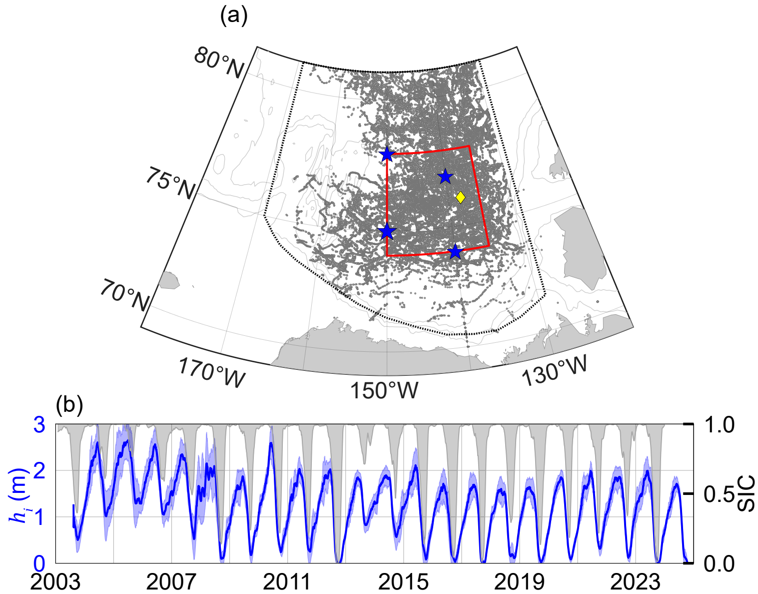

Figure 7. a) Map of the Beaufort Gyre region (BGR; black) and Central Canada Basin (CCB; red). Gray dots indicate locations of hydrographic observations from ITP and Beaufort Gyre Observing System (BGOS)/Joint Ice Ocean Study (JOIS) CTD casts. Blue stars indicate the location of the BGOS moorings. The yellow diamond indicates the location of the oceanographic profiles in Figure 8. b) Timeseries of mean sea ice thickness (blue) and SIC (gray) in the CCB from 2005 through 2023. These observations are derived from ice draft measurements via upward-looking sonar (ULS) on the BGOS moorings and the Nimbus-7 SMMR and DMSP SSM/I-SSMIS Passive Microwave Data Version 2 (DiGirolamo et al., 2022).

from the surface. We assign mixed-layer depths an uncertainty of ± 1 m reflecting the 1 m binned data. An additional source of uncertainty arises from computing N^2 as a centered difference between adjacent grid points, which offsets the mixed-layer base by up to half a bin. We therefore conservatively estimate a total uncertainty of 1 to 2 m. To compute a density difference, $\Delta\rho$ between the mixed layer and its base, we subtract the mean mixed-layer density ($\overline{\rho}$) from the density $\sim$1 m below the depth of N^2_m. This depth is at approximately the midpoint of the stratified interface beneath the mixed layer and provides a representative measure of the density of fluid being entrained (i.e., it captures the characteristic potential energy barrier to mixed-layer deepening).

We use sea-ice thickness observations to estimate the seasonal evolution of buoyancy fluxes. Upward-looking sonar (ULS) data (Krishfield et al., 2014) from four BGOS moorings provide continuous in situ ice draft measurements at locations within and bounding the CCB (blue stars, Figure 7a) over our study period. Ice thickness is inferred from ULS draft via a conversion factor of 1.123, with the resulting thickness estimated to be accurate within $\pm$10 cm (Figure 7b Melling et al., 1995; Krishfield et al., 2014). Between each of the moorings, there is a mean spatial standard deviation of 0.2 m for the 2003–2023 period. Since we aim to estimate buoyancy fluxes in the CCB, the metric of interest is the ice-thickness evolution, dh_i/dt. The average standard deviation of dh_i/dt is 1.0$\pm$0.1 cm day^{-1} between each of the moorings. From 1979–2023, May sea-ice volume (i.e.,

https://doi.org/10.5194/egusphere-2026-3283
Preprint. Discussion started: 3 August 2026

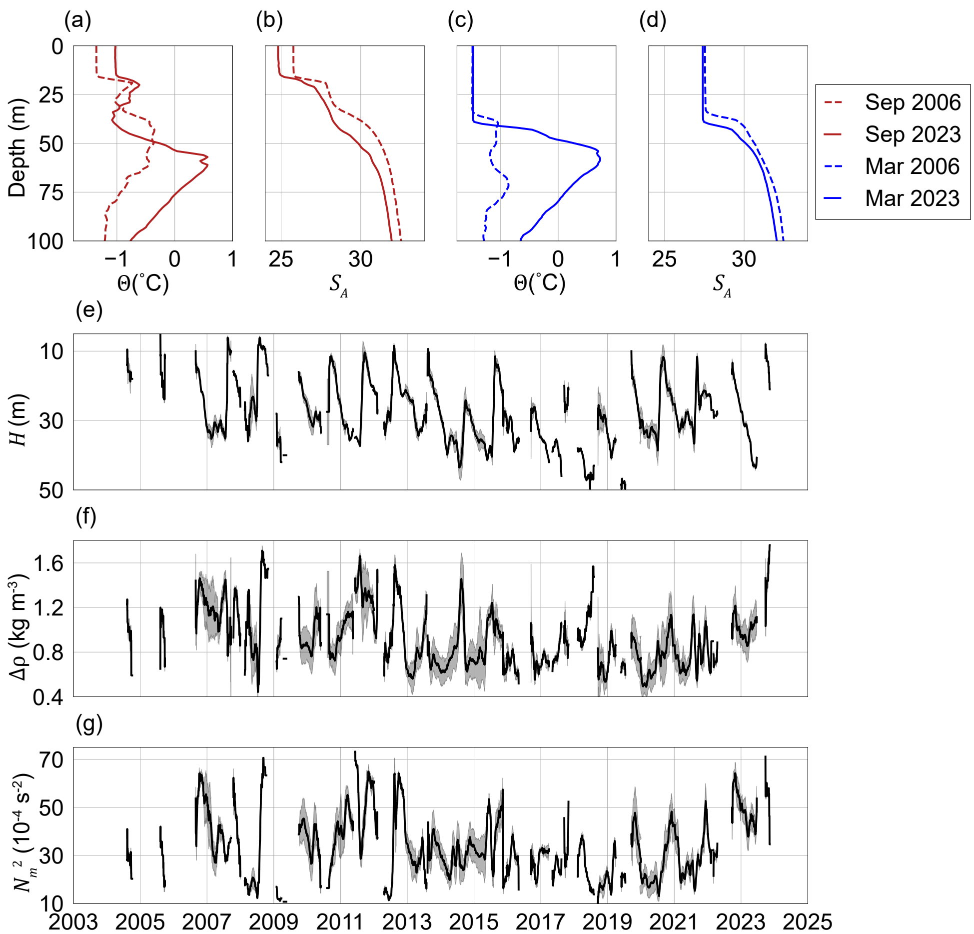

Figure 8. September profiles of a) conservative temperature (Θ) and b) absolute salinity (S_A) from 2006 (dashed) and 2023 (solid). March profiles of c) conservative temperature and d) absolute salinity from 2006 (dashed) and 2023 (solid). Profiles were taken from the location of the yellow diamond in Figure 7. 30-day running mean timeseries of e) mixed-layer thickness (H), f) density difference across the base of the mixed layer ($\Delta\rho$), and g) the maximum buoyancy frequency (N_m^2) in the central Canada Basin (CCB) from 2003–2023. Shading indicates one standard deviation for all profiles in a day.

at the end of the growing season) has declined more slowly than September sea-ice volume, a trend attributed to increased sea-ice growth rates of $\sim$1 cm per year over the broader Canada Basin (Bailey and Timmermans, 2025).

4.2 Observed monthly mean mixed-layer properties and seasonal evolution

Seasonally, the mixed layer is shallowest ($\lesssim$20 m) and freshest in September (Figure 8a,b) and deepens (to $\sim$40 m) and salinifies through March (Figure 8c,d). From 2003 through 2019, the CCB mixed layer has deepened by 1.1 ± 0.1 $\mathrm{m\,year^{-1}}$ (Figure 8e). After 2019, the mixed layer has exhibited a shoaling tendency, which coincides with a decrease in freshwater and heat

https://doi.org/10.5194/egusphere-2026-3283
Preprint. Discussion started: 3 August 2026

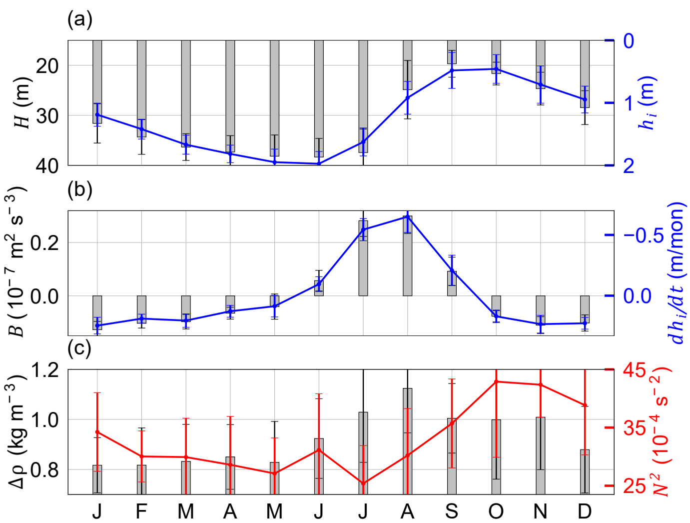

Figure 9. Monthly mean a) mixed-layer thickness (H) and sea-ice thickness (h_i, blue), b) buoyancy flux (B) and change in sea-ice thickness (dh_i/dt, blue), and c) density difference across the base of the mixed-layer ($\Delta\rho$) and the maximum buoyancy frequency (N_m^2, red) in the CCB for the 2003–2023 period. Error bars indicate one median absolute deviation within the CCB.

content in the upper ocean (Timmermans et al., 2025). If we consider monthly trends, there are statistically significant linear trends in April–December, when the mixed layer has become between ∼0.5–2.0 m deeper per year in any given month over the 2003–2019 period (Figure S9a). Cole and Stadler (2019) reported a 9 m increase in January–May mixed-layer thickness from 2006–2017 in the BGR, driven by changes in April–May values. Over 2003–2019, we similarly find no significant change in mixed-layer depth in January–March (Figure S9a).

Sea ice thickness in the CCB has a seasonal cycle consistent with seasonal mixed layer depth evolution, with maximum thicknesses of ∼2 m in May/June and the thinnest ice (∼0.5 m) in September (Figure 9a). There is a general decrease in sea-ice thickness across all months for the 2003–2019 period in the CCB (Figure S9a). After 2019, there are no significant changes in sea-ice thickness over the CCB (Figure 7b). From June through September, sea-ice ablation (hereafter referred to simply as melt) releases freshwater into the surface ocean (Figure 9b). Over the 2003–2019 period, we see a statistically significant increase in the rate of sea-ice melt (and the associated positive buoyancy fluxes) in September (Figure S9b). For the rest of the year, sea-ice growth releases brine and reduces the buoyancy of the surface ocean (Figure 9b). There are no significant changes in sea-ice growth over the 2003–2019 period (Figure S9b). Seasonal ice growth/melt results in a seasonal buoyancy flux that could contribute to changes in mixed layer depth. This will be explored in the next section.

Before quantifying mixed-layer entrainment, we first need to understand the seasonal evolution of mixed-layer stability, which is represented by both $\Delta\rho$ and N_m^2. Interannually, there has not been a clear trend in either $\Delta\rho$ or N_m^2 (Figure 8f,g). Over the course of a seasonal cycle, we find the density difference across the mixed-layer base ($\Delta\rho$) does not track the maximum buoyancy frequency (N_m^2), as would be expected if the density interface at the base of the mixed layer did not change in

https://doi.org/10.5194/egusphere-2026-3283
Preprint. Discussion started: 3 August 2026

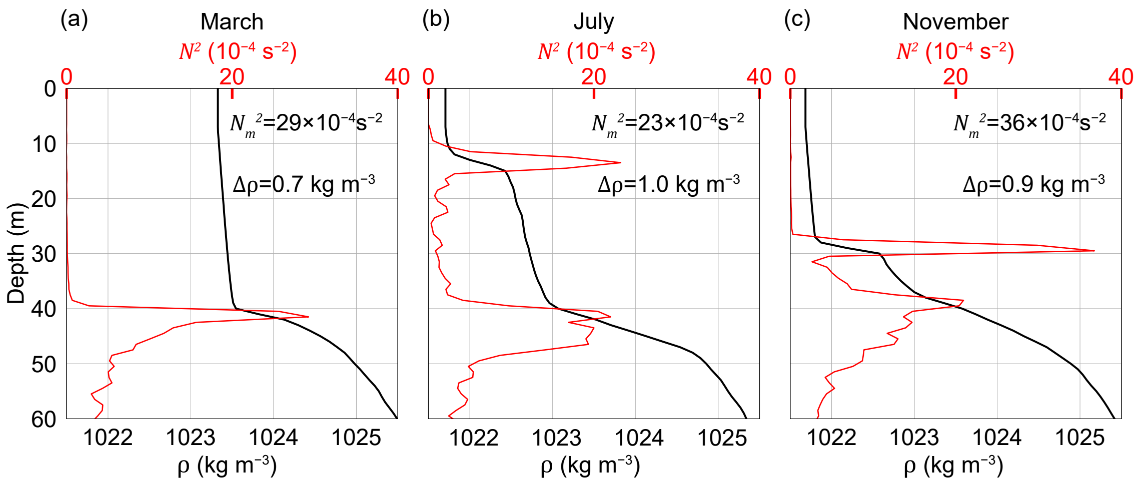

Figure 10. Profiles of density (ρ; black) and buoyancy frequency (N^2; red) for a) March, b) July, and c) November. All profiles were taken from ITP data in the CCB in 2014. The maximum buoyancy frequency (N_m^2) and density difference across the mixed layer ($\Delta\rho$) and its base are given for each profile.

thickness (Figure 9c). $\Delta\rho$ is smallest around January through May when mixed layers are deepest and most dense (Figure 9a,c). Throughout this season, larger values of N_m^2 coincide with relatively small values of $\Delta\rho$, suggesting mixed-layer entrainment via mechanical scouring thins the density interface at the mixed-layer base (Figure 10a). From June–August, $\Delta\rho$ increases with the onset of the melt season and the mixed layer shoals (Figure 9a,c); relatively small values of N_m^2 coincide with larger $\Delta\rho$, suggesting freshwater input to the surface ocean and weaker mechanical mixing allows for diffusion to thicken the density interface at the mixed layer base (Figure 10b). The coupled evolution of $\Delta\rho$ and N_m^2 hints at the differing influences of mechanical entrainment and surface buoyancy fluxes on mixed-layer evolution that we will now explore.

4.3 Quantifying mechanisms of mixed-layer deepening

Observations of mixed-layer thickness show a strong seasonality (Figure 9a) and a general trend towards a deeper mixed-layer until 2019 (Figure 8e and S9a). We aim to characterize and quantify the relative contributions of mechanical mixing and surface buoyancy forcing to both the seasonality and long-term trends in mixed-layer thickness.

Mixed-layer entrainment, w_e, may be estimated due to both surface stresses and buoyancy-fluxes (which may also shoal the mixed layer). Stigebrandt (1981, 1985) show that the rate of mixed-layer deepening can be quantified via a vertical entrainment velocity, w_e, given by

$$w_e = w_e^\tau + w_e^B = \frac{2m_0\rho_0 u_*^3}{g\Delta\rho H} - C\frac{B}{g\Delta\rho/\rho_0}, \tag{4}$$

where m_0 is a constant (empirical) mixing efficiency taken to be 0.6 (Stigebrandt, 1981, 1985), u_* is a frictional velocity calculated from the surface stress ($u_* = \sqrt{|\tau|/\rho_0}$), g is the gravitational acceleration, B is buoyancy flux and C is a non-dimensional empirical constant. The first term of (4), w_e^τ, represents mixed-layer entrainment due to stress applied at the

https://doi.org/10.5194/egusphere-2026-3283
Preprint. Discussion started: 3 August 2026

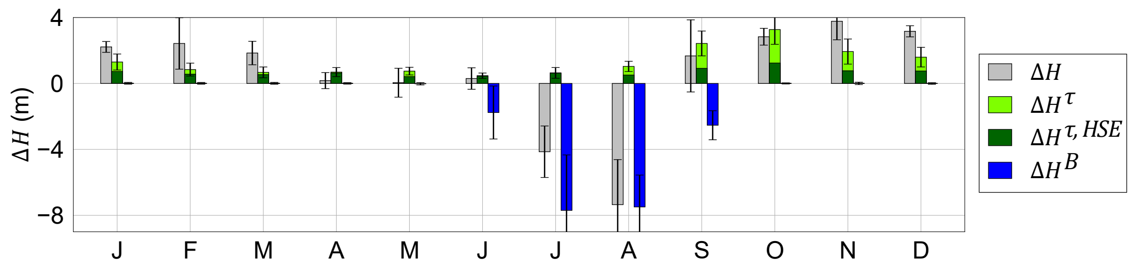

Figure 11. Climatology of monthly total observed mixed-layer thickness change (ΔH, gray), stress-induced mixed-layer thickness change (ΔH^{τ}, light green), stress-induced mixed-layer thickness change from HSEs ($\Delta H^{\tau,HSE}$, dark green), and buoyancy-driven changes (ΔH^{B}, blue) in the Central Canada Basin (CCB) for the 2003–2023 period from (4). Total monthly changes are calculated as $\Delta H = \int_{month} w_e dt$ for each term. Error bars indicate one median absolute deviation within the CCB.

surface, and is based on laboratory experiments and energetic arguments (Turner, 1968; Kato and Phillips, 1969). The second term, w_e^B, represents mixed-layer entrainment due to buoyancy fluxes, where B can be positive or negative. Here, we only consider buoyancy fluxes that arise from sea ice growth or melt. If $B > 0$, C is set to 1, while for $B < 0$, C is set to 0.05 (the release of dense brine leads to convective mixing); details are given by Farmer (1975); Stigebrandt (1981). The buoyancy flux, B, from a change in ice thickness, dh_i/dt, can be expressed as

$$B = g\beta \frac{\rho_i}{\rho_0}(\overline{S} - S_i)\frac{dh_i}{dt} \tag{5}$$

(see Cavalieri and Martin, 1994; Worster and Rees Jones, 2015), where $\rho_i = 900\ \mathrm{kg\,m^{-3}}$ is the density of sea ice, $\beta = 8 \times 10^{-4}$ is the coefficient of haline contraction, $\overline{S}$ is the mean salinity of the mixed layer, and $S_i = 9$ is the salinity of sea ice. We solve (4) and (5) iteratively to calculate the daily change in mixed-layer depth as a function of the timeseries of surface stress, the density gradient across the base of the mixed layer, sea ice thickness, and average mixed-layer salinity.

The parameterization (4) has been shown to reasonably capture mixed layer changes, where the largest discrepancies may be due to the influence of lateral flows (e.g., convergence/divergence of water as a result of surface-ocean stress curl and the subsequent vertical Ekman pumping) not captured in the 1D framework (Stigebrandt, 1985; Björk, 1989; Hordoir et al., 2022). Furthermore, the relationship does not account for mixed-layer deepening driven by shear instabilities at the base of the mixed layer; the effect is included in the Price-Weller-Pinkel (PWP) one-dimensional model (Price et al., 1986), which has been used to explore mixed-layer processes in the BGR (e.g., Toole et al., 2010; Zhong et al., 2025). Nevertheless, (4) is a reasonable parameterization of mixed-layer entrainment when averaging over multiple inertial periods (Price et al., 1978). Although other uncertainties arise (in the choice of m_0 and C, for example), this representation of mixed-layer deepening reproduces a similar depth evolution to more complex models of the Arctic Ocean, such as the three-layer model used in Dukhovskoy et al. (2006).

To understand the general seasonal influence of each of the terms in equation (4), we take the sum of each term in equation (4) over any given month, then take the interannual mean (Figure 11). For observed changes in mixed-layer thickness, we fit a linear regression to all daily mixed-layer thickness data for any given month.

https://doi.org/10.5194/egusphere-2026-3283
Preprint. Discussion started: 3 August 2026

During the ice growth season (October through May), w_e^B remains weakly positive and small (Figure 11a). Stress-induced mixed-layer deepening w_e^τ is largest in September through January. This seasonal maximum is particularly pronounced in the early winter months: mechanical deepening in October through December is twice that in January through March. When comparing these estimated values to observed mixed-layer evolution during the deepening season (October through March), we find that stress-driven entrainment can account for an average of 65% of mixed-layer deepening, while buoyancy-driven entrainment contributes only 7% (Figure 11a). Hence, surface momentum transfer plays a larger role in seasonal mixed-layer deepening than convection in the CCB (Figure 11).

Since mechanical mixing is a dominant contributor to seasonal mixed-layer deepening, we now seek to evaluate the role of episodic HSEs. On average, each HSE results in 0.8 ± 0.5 m of mechanical deepening. Despite occurring only 7% of the time, these episodic events account for approximately 28% of all stress-induced mixing in the 2003–2023 period. This contribution becomes even more pronounced in April–July, when HSEs account for an average of $\sim$68% of stress-driven entrainment (Figure 11). This suggests that HSEs are a critical contributor to the seasonality of mixed-layer thickness, particularly in spring and early summer.

In the melt season, mechanical entrainment is secondary to buoyancy forcing. During July and August, w_e^B exhibits large negative values, indicating strong shoaling driven by freshwater release from ice melt (Figure 11). Our estimates of shoaling as a result of ice melt are typically larger ($\sim$3 m per month on average) than observed decreases in mixed-layer thickness in the melt season (Figure 11). The implicit assumption in shoaling estimates from w_e^B is that the freshwater released from ice melt remains in the CCB, which may be the source of the shoaling overestimate (e.g., see the tracer trajectories in Proshutinsky et al. (2019)).

Beyond these seasonal patterns, long-term trends reveal that the mechanical forcing controlling mixed-layer depth is intensifying. We have shown that surface stress has increased during ice-covered months over 2003–2023, with particularly strong trends in November and December ($\sim$0.001 $\mathrm{N\,m^{-2}\,year^{-1}}$; Figure 5c). These increasing surface stress trends have direct consequences for mixed-layer evolution. The enhanced momentum transfer has driven increased mechanical entrainment of $\sim$1.5 m per decade in November and $\sim$1 m per decade in December over 2003–2019 (Figure S10b). This increased deepening equates to approximately 20% of the $\sim$7 m per decade in November and $\sim$6 m per decade in December of mixed-layer deepening that we observed from 2003–2019 (Figure S9a). Furthermore, there is no clear change in either mechanical entrainment or surface buoyancy forcing for the months with the largest interannual increases in observed mixed-layer depth (i.e., April–August, Figures S9a and S10). The drivers of the bulk of the mixed-layer thickness trend remain unconstrained.

5 Summary and Discussion

Our investigation of monthly and interannual variability in surface ocean stress in the CCB over 2003 to 2023 has shown a statistically significant linear increase in surface stress magnitude of approximately 0.007 ± 0.001 $\mathrm{N\,m^{-2}}$ per decade, with the most pronounced increases ($\sim$0.01 $\mathrm{N\,m^{-2}}$ per decade) in November–December. These months coincide with the annual maximum surface stress magnitudes occurring in September through December. The increases in surface stress are primarily attributed to increased sea-ice mobility (consistent with previous studies, Petty et al. (2016); Martin et al. (2014)), where sea ice has become more responsive to the largely unchanged wind forcing in the 2003–2023 period. Our assessment of high-stress events (HSEs) indicates no change in the characteristics of individual events, though there has been an increase in their frequency, and a consequent increase in the time-integrated stress of 0.54 $\pm$ 0.45 $\mathrm{N\,m^{-2}}$ per decade associated with all HSEs, over the 2003–2023 period.

We have further investigated the influence of surface-ocean stresses and greater sea-ice mobility on monthly and interannual variability of mixed-layer depth. Overall, we observe a general mixed layer deepening (linear trend of $\sim$1.1 $\mathrm{m\,yr^{-1}}$) in the first part of the record, from 2003–2019. This is superimposed on a strong seasonal cycle (shallowest in September, $\sim$20 m, and deepest, $\sim$40 m, in May). For April through December, each month has a statistically significant linear trend to thicker mixed layers over the 2003–2019 period, with the largest increases occurring in the months of May through August (linear trends between 1–2 $\mathrm{m\,year^{-1}}$). After 2019, the mixed layer tends to shoal overall, with a linear trend of $\sim$-0.4 $\mathrm{m\,year^{-1}}$.

We have employed a 1D energy-balance entrainment parameterization to estimate that stress-induced entrainment can account for $\sim$65% of the observed mixed-layer deepening in any given year in October through March, while buoyancy-driven entrainment (i.e., brine rejection) accounts for only $\sim$7% of the observed deepening in these months. HSEs have a disproportionately large influence on stress-induced mixed-layer deepening relative to their occurrence. In October through March, HSEs account for about 38% of all stress-induced deepening, while only occurring during 8% of the time over the 2003–2023 period. For all months, HSES are responsible for $\sim$28% of mechanical deepening although they only occur during 7% of the time. This picture of seasonal mixed-layer deepening in the CCB differs from seasonal deepening being primarily driven by convection associated with sea-ice growth/brine rejection with occasional storm-driven mechanical deepening (e.g., Peralta-Ferriz and Woodgate, 2015). The 1D energy balance indicates that sea-ice melt is the dominant driver of mixed-layer shoaling in June–August, with the model estimate approximately twice the observed shoaling in July and approximately equal to it in August.

Approximately 28% of the average seasonal deepening in October–March is not due to stress-induced entrainment or brine-driven convection. As such, other processes have non-negligible contributions to observed mixed-layer deepening. For example, the lateral convergence of water in the mixed layer, giving rise to Ekman pumping, plays an important role in this seasonality. Ekman downwelling has a seasonal peak of $\sim$0.8 m in September–December, which has been previously described in the region (Figure S10d; e.g., Meneghello et al., 2018). During October through March, when stress-induced entrainment is the dominant process that drives seasonal mixed-layer deepening, Ekman pumping can account for $\sim$21% of the total deepening that occurs (Figure S10). Similarly, in other months of the year, Ekman pumping cannot explain the observed mixed-layer depth changes.

Interannual increases in surface stress imply an increase in mechanical entrainment of $\sim$0.8 m per decade in November and December over the 2003–2023 period. This has potentially significant implications for ocean-to-ice heat fluxes as the relatively warm Pacific Summer Water layer (PSW) resides immediately beneath the mixed layer in the Canada Basin. Given some rate of mixed-layer deepening w_e, the corresponding heat flux can be estimated as $F_H = \rho_0 c_p w_e \Delta T$, where ΔT is the temperature difference between the mixed layer and the warmer water immediately below. Typical values of ΔT are between $\sim$0.3 and

0.5 °C, estimated the same way as $\Delta\rho$. A mixed layer deepening of 1 m over 1 month (i.e., the approximate increase in observed mixed-layer deepening in November and December over the 2003-2023 period) would therefore correspond to heat flux of ~0.5–0.8 $\mathrm{W\,m^{-2}}$, comparable to the observed ~0.87 $\mathrm{W\,m^{-2}}$ increase in wintertime ocean-to-ice heat fluxes between the 2006–2012 and 2013–2018 periods of Zhong et al. (2022). This increase in heat flux alone would account for up to ~0.7 cm of sea ice melt in one month.

The increased mechanical deepening in November/December inferred from surface stress increases over 2003–2019 is only ~20% of the observed increase in mixed-layer thickness in these months over the same period. Neither changes in mechanical entrainment nor buoyancy forcing can explain the observed increases in mixed-layer thickness from 2003–2019 in all other months with statistically significant trends (April–October). Further, we do not see any significant change in Ekman pumping that can account for the observed deepening of the mixed layer (Figure S10d). While it is noteworthy that increases in mixed-layer thickness from 2003–2019, as well as the subsequent shoaling from 2020–2023, show a similar temporal pattern to the interannual changes in freshwater and heat content in the region (see Timmermans et al., 2025), the net effect of Ekman pumping, dissipative processes, and buoyancy sources is complicated.

As the Arctic sea ice pack continues to thin and retreat, it can be expected that sea ice mobility and surface ocean stress will continue to increase. On the other hand, model projections indicate that winds will likely weaken in the future, which may act to decrease momentum transfer within the atmosphere-ice-ocean system (Athanase et al., 2025). These changes should continue to be explored with respect to surface-ocean stresses and mixed-layer entrainment, particularly given the importance of stress-driven mixing on ocean-to-ice heat fluxes. Overall, these results highlight the importance of continuous, high-quality sea ice and oceanographic observations for monitoring changes in the Arctic system.

Data availability. Sea ice velocity and concentration data are from the National Snow and Ice Data Center and are available at https://nsidc.org/data/nsidc-0116/versions/4 and https://nsidc.org/data/nsidc-0051/versions/2, respectively (Tschudi et al., 2019; DiGirolamo et al., 2022). Winds are from the ECMWF reanalysis data product (ERA5) and are available from the Copernicus Climate Data Store at https://doi.org/10.24381/cds.adbb2d47 (Hersbach et al., 2018). Dynamic ocean topography data for 2003-2020 were provided by the Centre for Polar Observation and Modelling, University College London and are available at www.cpom.ucl.ac.uk/dynamic_topography (Armitage et al., 2016, 2017; Lin et al., 2023). Dynamic ocean topography data for 2021-2023 were provided by the National Snow and Ice Data Center and are available at https://nsidc.org/data/atl23/versions/2 (Morison et al., 2025). While these products are available individually, the 2003 – 2023 DOT, surface ocean stress, and Ekman pumping products will be available on GitHub or the Arctic Data Center, pending Margevich et al. being accepted. The Ice-Tethered Profiler data were collected and made available by the Ice-Tethered Profiler Program (Krishfield et al., 2008; Toole et al., 2011) based at the Woods Hole Oceanographic Institution (https://www2.whoi.edu/site/itp/) and are available at https://doi.org/10.7289/v5mw2f7x. CTD and Upward-looking sonar (ULS) data were collected and made available by the Beaufort Gyre Exploration Program (https://www2.whoi.edu/site/beaufortgyre/) in collaboration with the Joint Ice Ocean Study (JOIS) program with researchers from Fisheries and Oceans Canada at the Institute of Ocean Sciences (IOS). ITP and CTD data are also available at the NSF Arctic Data Center (https://arcticdata.io/).

https://doi.org/10.5194/egusphere-2026-3283
Preprint. Discussion started: 3 August 2026

Author contributions. EB and MT designed the study. AM provided processed DOT and Ekman pumping data. EB made the analyses and the figures. All authors contributed to the interpretation of the results. EB wrote the manuscript with inputs from MT and AM.

Competing interests. The authors declare that they have no conflict of interest.

Acknowledgements. Funding for this study was provided by the Office of Naval Research (ONR) Multidisciplinary University Research Initiatives Program and the National Science Foundation, Division of Polar Programs.

https://doi.org/10.5194/egusphere-2026-3283
Preprint. Discussion started: 3 August 2026

References

Armitage, T. W. K., Bacon, S., Ridout, A. L., Thomas, S. F., Aksenov, Y., and Wingham, D. J.: Arctic sea surface height variability and change from satellite radar altimetry and GRACE, 2003–2014, Journal of Geophysical Research: Oceans, 121, 4303–4322, https://doi.org/10.1002/2015JC011579, 2016.

Armitage, T. W. K., Bacon, S., Ridout, A. L., Petty, A. A., Wolbach, S., and Tsamados, M.: Arctic Ocean surface geostrophic circulation 2003–2014, The Cryosphere, 11, 1767–1780, https://doi.org/10.5194/tc-11-1767-2017, 2017.

Athanase, M., Köhler, R., Heuzé, C., Lévine, X., and Williams, R.: The Arctic Beaufort Gyre in CMIP6 Models: Present and Future, Journal of Geophysical Research: Oceans, 130, e2024JC021 873, https://doi.org/10.1029/2024JC021873, 2025.

Babb, D. G., Galley, R. J., Howell, S. E. L., Landy, J. C., Stroeve, J. C., and Barber, D. G.: Increasing Multiyear Sea Ice Loss in the Beaufort Sea: A New Export Pathway for the Diminishing Multiyear Ice Cover of the Arctic Ocean, Geophysical Research Letters, 49, e2021GL097 595, https://doi.org/10.1029/2021GL097595, 2022.

Bailey, E. and Timmermans, M.: Investigating the Relative Roles of Dynamics and Thermodynamics in Sea-Ice Volume Changes in the Canada Basin, Journal of Geophysical Research: Oceans, 130, e2024JC022 075, https://doi.org/10.1029/2024JC022075, 2025.

Björk, G.: A One-Dimensional Time-Dependent Model for the Vertical Stratification of the Upper Arctic Ocean, Journal of Physical Oceanography, 19, 52–67, https://doi.org/10.1175/1520-0485(1989)019<0052:AODTDM>2.0.CO;2, 1989.

Brenner, S., Rainville, L., Thomson, J., Cole, S., and Lee, C.: Comparing Observations and Parameterizations of Ice-Ocean Drag Through an Annual Cycle Across the Beaufort Sea, Journal of Geophysical Research: Oceans, 126, e2020JC016 977, https://doi.org/10.1029/2020JC016977, 2021.

Cavalieri, D. J. and Martin, S.: The contribution of Alaskan, Siberian, and Canadian coastal polynyas to the cold halocline layer of the Arctic Ocean, Journal of Geophysical Research: Oceans, 99, 18 343–18 362, https://doi.org/10.1029/94JC01169, 1994.

Cole, S. T. and Stadler, J.: Deepening of the Winter Mixed Layer in the Canada Basin, Arctic Ocean Over 2006–2017, Journal of Geophysical Research: Oceans, 124, 4618–4630, https://doi.org/10.1029/2019JC014940, 2019.

Cole, S. T., Toole, J. M., Lele, R., Timmermans, M.-L., Gallaher, S. G., Stanton, T. P., Shaw, W. J., Hwang, B., Maksym, T., Wilkinson, J. P., Ortiz, M., Graber, H., Rainville, L., Petty, A. A., Farrell, S. L., Richter-Menge, J. A., and Haas, C.: Ice and ocean velocity in the Arctic marginal ice zone: Ice roughness and momentum transfer, Elementa: Science of the Anthropocene, 5, 55, https://doi.org/10.1525/elementa.241, 2017.

Dewey, S., Morison, J., Kwok, R., Dickinson, S., Morison, D., and Andersen, R.: Arctic Ice-Ocean Coupling and Gyre Equilibration Observed With Remote Sensing, Geophysical Research Letters, 45, 1499–1508, https://doi.org/10.1002/2017GL076229, 2018.

DiGirolamo, N., Parkinson, C., Cavalieri, D., Gloersen, P., and Zwally, H.: Sea Ice Concentrations from Nimbus-7 SMMR and DMSP SSM/I-SSMIS Passive Microwave Data, Version 2, https://doi.org/10.5067/MPYG15WAA4WX, 2022.

Dukhovskoy, D., Johnson, M., and Proshutinsky, A.: Arctic decadal variability from an idealized atmosphere-ice-ocean model: 1. Model description, calibration, and validation, Journal of Geophysical Research: Oceans, 111, 2004JC002 821, https://doi.org/10.1029/2004JC002821, 2006.

Farmer, D. M.: Penetrative convection in the absence of mean shear, Quarterly Journal of the Royal Meteorological Society, 101, 869–891, https://doi.org/10.1002/qj.49710143011, 1975.

Geernaert, G.: On the importance of the drag coefficient in air-sea interactions, Dynamics of Atmospheres and Oceans, 11, 19–38, https://doi.org/10.1016/0377-0265(87)90012-1, 1987.

https://doi.org/10.5194/egusphere-2026-3283
Preprint. Discussion started: 3 August 2026

Graham, R. M., Cohen, L., Ritzhaupt, N., Segger, B., Graversen, R. G., Rinke, A., Walden, V. P., Granskog, M. A., and Hudson, S. R.: Evaluation of Six Atmospheric Reanalyses over Arctic Sea Ice from Winter to Early Summer, Journal of Climate, 32, 4121–4143, https://doi.org/10.1175/JCLI-D-18-0643.1, 2019.

Hersbach, H., Bell, B., Berrisford, P., Biavati, G., Horányi, A., Muñoz Sabater, J., Nicolas, J., Peubey, C., Radu, R., Rozum, I., Schepers, D., Simmons, A., Soci, C., and Thépaut, J.-N.: ERA5 hourly data on single levels from 1940 to present, https://doi.org/10.24381/CDS.ADBB2D47, 2018.

Hordoir, R., Skagseth, , Ingvaldsen, R. B., Sandø, A. B., Löptien, U., Dietze, H., Gierisch, A. M. U., Assmann, K. M., Lundesgaard, , and Lind, S.: Changes in Arctic Stratification and Mixed Layer Depth Cycle: A Modeling Analysis, Journal of Geophysical Research: Oceans, 127, e2021JC017 270, https://doi.org/10.1029/2021JC017270, 2022.

Kato, H. and Phillips, O. M.: On the penetration of a turbulent layer into stratified fluid, Journal of Fluid Mechanics, 37, 643–655, https://doi.org/10.1017/S0022112069000784, 1969.

Krishfield, R., Toole, J., Proshutinsky, A., and Timmermans, M.-L.: Automated Ice-Tethered Profilers for Seawater Observations under Pack Ice in All Seasons, Journal of Atmospheric and Oceanic Technology, 25, 2091–2105, https://doi.org/10.1175/2008JTECHO587.1, 2008.

Krishfield, R. A., Proshutinsky, A., Tateyama, K., Williams, W. J., Carmack, E. C., McLaughlin, F. A., and Timmermans, M.: Deterioration of perennial sea ice in the Beaufort Gyre from 2003 to 2012 and its impact on the oceanic freshwater cycle, Journal of Geophysical Research: Oceans, 119, 1271–1305, https://doi.org/10.1002/2013JC008999, 2014.

Large, W. G. and Pond, S.: Open Ocean Momentum Flux Measurements in Moderate to Strong Winds, Journal of Physical Oceanography, 11, 324–336, https://doi.org/10.1175/1520-0485(1981)011<0324:OOMFMI>2.0.CO;2, 1981.

Lin, P., Pickart, R. S., Heorton, H., Tsamados, M., Itoh, M., and Kikuchi, T.: Recent state transition of the Arctic Ocean's Beaufort Gyre, Nature Geoscience, 16, 485–491, https://doi.org/10.1038/s41561-023-01184-5, 2023.

Liu, C. and Yu, L.: Satellite-Based Evidence of Winter Intensification of Ocean Surface Stress and Ekman Downwelling in the Beaufort Gyre Since the 2010s, Journal of Geophysical Research: Oceans, 130, e2025JC022 521, https://doi.org/10.1029/2025JC022521, 2025.

Margevich, A., Timmermans, M.-L., and Danielson, S.: Drivers of Ekman Pumping and Subduction in the Northern Chukchi Sea and Implications for Interior Beaufort Gyre Waters, Submitted to Journal of Geophysical Research: Oceans.

Martin, T., Steele, M., and Zhang, J.: Seasonality and long-term trend of Arctic Ocean surface stress in a model, Journal of Geophysical Research: Oceans, 119, 1723–1738, https://doi.org/10.1002/2013JC009425, 2014.

Mcphee, M. G.: An analysis of pack ice drift in summer, Sea ice processes and models, pp. 62–75, 1980.

Melling, H., Johnston, P. H., and Riedel, D. A.: Measurements of the underside topography of sea ice by moored subsea sonar, Journal of Atmospheric and Oceanic Technology, 12, 589–602, 1995.

Meneghello, G., Marshall, J., Cole, S. T., and Timmermans, M.: Observational Inferences of Lateral Eddy Diffusivity in the Halocline of the Beaufort Gyre, Geophysical Research Letters, 44, https://doi.org/10.1002/2017GL075126, 2017.

Meneghello, G., Marshall, J., Timmermans, M.-L., and Scott, J.: Observations of Seasonal Upwelling and Downwelling in the Beaufort Sea Mediated by Sea Ice, Journal of Physical Oceanography, 48, 795–805, https://doi.org/10.1175/JPO-D-17-0188.1, 2018.

Morison, J., Hancock, D., Dickinson, S., Robbins, J., and Roberts, L.: ATLAS/ICESat-2 L3B Monthly 3-Month Gridded Dynamic Ocean Topography, Version 2, https://doi.org/10.5067/ATLAS/ATL23.002, 2025.

Muilwijk, M., Hattermann, T., Martin, T., and Granskog, M. A.: Future sea ice weakening amplifies wind-driven trends in surface stress and Arctic Ocean spin-up, Nature Communications, 15, 6889, https://doi.org/10.1038/s41467-024-50874-0, 2024.

https://doi.org/10.5194/egusphere-2026-3283
Preprint. Discussion started: 3 August 2026

Peng, L., Zhang, X., Kim, J., Cho, K., Kim, B., Wang, Z., and Tang, H.: Role of Intense Arctic Storm in Accelerating Summer Sea Ice Melt: An In Situ Observational Study, Geophysical Research Letters, 48, e2021GL092 714, https://doi.org/10.1029/2021GL092714, 2021.

Peralta-Ferriz, C. and Woodgate, R. A.: Seasonal and interannual variability of pan-Arctic surface mixed layer properties from 1979 to 2012 from hydrographic data, and the dominance of stratification for multiyear mixed layer depth shoaling, Progress in Oceanography, 134, 19–53, https://doi.org/10.1016/j.pocean.2014.12.005, 2015.

Petty, A. A., Hutchings, J. K., Richter-Menge, J. A., and Tschudi, M. A.: Sea ice circulation around the Beaufort Gyre: The changing role of wind forcing and the sea ice state, Journal of Geophysical Research: Oceans, 121, 3278–3296, https://doi.org/10.1002/2015JC010903, 2016.

Price, J. F., Mooers, C. N. K., and Van Leer, J. C.: Observation and Simulation of Storm-Induced Mixed-Layer Deepening, Journal of Physical Oceanography, 8, 582–599, https://doi.org/10.1175/1520-0485(1978)008<0582:OASOSI>2.0.CO;2, 1978.

Price, J. F., Weller, R. A., and Pinkel, R.: Diurnal cycling: Observations and models of the upper ocean response to diurnal heating, cooling, and wind mixing, Journal of Geophysical Research: Oceans, 91, 8411–8427, https://doi.org/10.1029/JC091iC07p08411, 1986.

Proshutinsky, A., Bourke, R. H., and McLaughlin, F. A.: The role of the Beaufort Gyre in Arctic climate variability: Seasonal to decadal climate scales, Geophysical Research Letters, 29, https://doi.org/10.1029/2002GL015847, 2002.

Proshutinsky, A., Krishfield, R., Timmermans, M., Toole, J., Carmack, E., McLaughlin, F., Williams, W. J., Zimmermann, S., Itoh, M., and Shimada, K.: Beaufort Gyre freshwater reservoir: State and variability from observations, Journal of Geophysical Research: Oceans, 114, 2008JC005 104, https://doi.org/10.1029/2008JC005104, 2009.

Proshutinsky, A., Krishfield, R., Toole, J. M., Timmermans, M., Williams, W., Zimmermann, S., Yamamoto-Kawai, M., Armitage, T. W. K., Dukhovskoy, D., Golubeva, E., Manucharyan, G. E., Platov, G., Watanabe, E., Kikuchi, T., Nishino, S., Itoh, M., Kang, S., Cho, K., Tateyama, K., and Zhao, J.: Analysis of the Beaufort Gyre Freshwater Content in 2003–2018, Journal of Geophysical Research: Oceans, 124, 9658–9689, https://doi.org/10.1029/2019JC015281, 2019.

Rainville, L. and Woodgate, R. A.: Observations of internal wave generation in the seasonally ice-free Arctic, Geophysical Research Letters, 36, 2009GL041 291, https://doi.org/10.1029/2009GL041291, 2009.

Serreze, M. C. and Barrett, A. P.: Characteristics of the Beaufort Sea High, Journal of Climate, 24, 159–182, https://doi.org/10.1175/2010JCLI3636.1, 2011.

Stern, H. L.: Regime Shift in Arctic Ocean Sea-Ice Extent, Geophysical Research Letters, 52, e2024GL114 546, https://doi.org/10.1029/2024GL114546, 2025.

Stigebrandt, A.: A Model for the Thickness and Salinity of the Upper Layer in the Arctic Ocean and the Relationship between the Ice Thickness and Some External Parameters, Journal of Physical Oceanography, 11, 1407–1422, https://doi.org/10.1175/1520-0485(1981)011<1407:AMFTTA>2.0.CO;2, 1981.

Stigebrandt, A.: A Model for the Seasonal Pycnocline in Rotating Systems with Application to the Baltic Proper, Journal of Physical Oceanography, 15, 1392–1404, https://doi.org/10.1175/1520-0485(1985)015<1392:AMFTSP>2.0.CO;2, 1985.

Stoll, P. J.: Background Data for: A global climatology of polar lows investigated for local differences and wind-shear environments, https://doi.org/10.18710/TVZDBF, 2022a.

Stoll, P. J.: A global climatology of polar lows investigated for local differences and wind-shear environments, Weather and Climate Dynamics, 3, 483–504, https://doi.org/10.5194/wcd-3-483-2022, 2022b.

Thoman, R. L., Moon, T. A., Druckenmiller, M. L., Askjaer, T. G., Ballinger, T. J., Bhatt, U. S., Berner, L. T., Bernhard, G. H., Bigalke, S., Bjerke, J. W., Bliss, A., Box, J. E., Brady, M., Brettschneider, B., Butler, A. H., Christiansen, H. H., Crawford, A., Decharme, B.,

https://doi.org/10.5194/egusphere-2026-3283
Preprint. Discussion started: 3 August 2026

Derksen, C., Divine, D., Elias Chereque, A., Epstein, H. E., Farrell, S., Fausto, R. S., Fettweis, X., Fioletov, V. E., Forbes, B. C., Frost, G. V. J., Gerland, S., Grooß, J.-U., Hanna, E., Hendricks, S., Howell, S., Ialongo, I., Isaksen, K., Jia, G., Johnsen, B., Kaleschke, L., Kim, S.-J., Labe, Z. M., Lader, R., Lakkala, K., Lara, M. J., Lee, S. H., Loomis, B. D., Luojus, K., Macander, M. J., Magnússon, R. , Mankoff, K. D., McClelland, J. W., Medley, B., Meier, W. N., Montesano, P. M., Mote, T. L., Motrøen Gjelten, H., Mudryk, L., Müller, R., Neigh, C. S. R., Nyland, K. E., Overland, J. E., Perovich, D. K., Petty, A., Phoenix, G. K., Poinar, K., Ricker, R., Romanovsky, V. E., Scheller, J. H., Serreze, M. C., Shiklomanov, A. I., Shiklomanov, N. I., Smith, B. E., Smith, S. L., Spencer, R. G. M., Streletskiy, D. A., Suslova, A., Svendby, T., Tank, S. E., Tian-Kunze, X., Tedesco, M., Timmermans, M.-L., Tømmervik, H., Tretiakov, M., Waigl, C. F., Walker, D. S. A., Walsh, J. E., Wang, M., Webster, M., Yang, D., and Zolkos, S.: The Arctic, Bulletin of the American Meteorological Society, 106, S300–S356, https://doi.org/10.1175/BAMS-D-25-0104.1, 2025.

Timmermans, M., Le Bras, I., O'Brien, J., Margevich, A., Macoun, P., Williams, B., and Zimmermann, S.: Introduction to the Special Collection on the Arctic Ocean's Changing Beaufort Gyre, Journal of Geophysical Research: Oceans, 130, e2025JC023 013, https://doi.org/10.1029/2025JC023013, 2025.

Timmermans, M.-L. and Toole, J. M.: The Arctic Ocean's Beaufort Gyre, Annual Review of Marine Science, 15, 223–248, https://doi.org/10.1146/annurev-marine-032122-012034, 2023.

Timmermans, M.-L., Toole, J., and Krishfield, R.: Warming of the interior Arctic Ocean linked to sea ice losses at the basin margins, Science Advances, 4, eaat6773, https://doi.org/10.1126/sciadv.aat6773, 2018.

Toole, J., Krishfield, R., Timmermans, M.-L., and Proshutinsky, A.: The Ice-Tethered Profiler: Argo of the Arctic, Oceanography, 24, 126–135, https://doi.org/10.5670/oceanog.2011.64, 2011.

Toole, J. M., Timmermans, M., Perovich, D. K., Krishfield, R. A., Proshutinsky, A., and Richter-Menge, J. A.: Influences of the ocean surface mixed layer and thermohaline stratification on Arctic Sea ice in the central Canada Basin, Journal of Geophysical Research: Oceans, 115, 2009JC005 660, https://doi.org/10.1029/2009JC005660, 2010.

Tschudi, M., Meier, W. N., Stewart, J. S., Fowler, C., and Maslanik, J.: Polar Pathfinder Daily 25 km EASE-Grid Sea Ice Motion Vectors, https://doi.org/10.5067/INAWUWO7QH7B, 2019.

Turner, J. S.: The influence of molecular diffusivity on turbulent entrainment across a density interface, Journal of Fluid Mechanics, 33, 639, https://doi.org/10.1017/S002211206800159X, 1968.

Worster, M. G. and Rees Jones, D. W.: Sea-ice thermodynamics and brine drainage, Philosophical Transactions of the Royal Society A: Mathematical, Physical and Engineering Sciences, 373, 20140 166, https://doi.org/10.1098/rsta.2014.0166, 2015.

Yang, J.: The Seasonal Variability of the Arctic Ocean Ekman Transport and Its Role in the Mixed Layer Heat and Salt Fluxes, Journal of Climate, 19, 5366–5387, https://doi.org/10.1175/JCLI3892.1, 2006.

Yang, J., Comiso, J., Krishfield, R., and Honjo, S.: Synoptic storms and the development of the 1997 warming and freshening event in the Beaufort Sea, Geophysical Research Letters, 28, 799–802, https://doi.org/10.1029/2000GL011896, 2001.

Yang, J., Comiso, J., Walsh, D., Krishfield, R., and Honjo, S.: Storm-driven mixing and potential impact on the Arctic Ocean, Journal of Geophysical Research: Oceans, 109, 2001JC001 248, https://doi.org/10.1029/2001JC001248, 2004.

Zhang, F., Pang, X., Lei, R., Zhai, M., Zhao, X., and Cai, Q.: Arctic sea ice motion change and response to atmospheric forcing between 1979 and 2019, International Journal of Climatology, 42, 1854–1876, https://doi.org/10.1002/joc.7340, 2022.

Zhang, J. and Rothrock, D. A.: Modeling Global Sea Ice with a Thickness and Enthalpy Distribution Model in Generalized Curvilinear Coordinates, Monthly Weather Review, 131, 845–861, https://doi.org/10.1175/1520-0493(2003)131<0845:MGSIWA>2.0.CO;2, 2003.

https://doi.org/10.5194/egusphere-2026-3283
Preprint. Discussion started: 3 August 2026

Zhang, J., Lindsay, R., Schweiger, A., and Steele, M.: The impact of an intense summer cyclone on 2012 Arctic sea ice retreat, Geophysical Research Letters, 40, 720–726, https://doi.org/10.1002/grl.50190, 2013.

Zhong, W., Steele, M., Zhang, J., and Zhao, J.: Greater Role of Geostrophic Currents in Ekman Dynamics in the Western Arctic Ocean as a Mechanism for Beaufort Gyre Stabilization, Journal of Geophysical Research: Oceans, 123, 149–165, https://doi.org/10.1002/2017JC013282, 2018.

Zhong, W., Cole, S. T., Zhang, J., Lei, R., and Steele, M.: Increasing Winter Ocean-to-Ice Heat Flux in the Beaufort Gyre Region, Arctic Ocean Over 2006–2018, Geophysical Research Letters, 49, e2021GL096 216, https://doi.org/10.1029/2021GL096216, 2022.

Zhong, W., Steele, M., Zhang, J., Su, J., and Zhao, J.: Weaker Seasonal Variation in Potential Energy Anomaly in the Upper Beaufort Gyre Favors the Upward Release of Subsurface Heat, Journal of Physical Oceanography, 55, 1051–1066, https://doi.org/10.1175/JPO-D-24-0205.1, 2025.